

Spatially resolved surface dissipation over metal and dielectric substrates

Martin Hérítier,[†] Raphael Pachlatko,[†] Ye Tao,[‡] John M. Abendroth,[†] Christian L. Degen,[†] and Alexander Eichler^{*,†}

[†]Laboratory for Solid State Physics, ETH Zürich, CH-8093 Zürich, Switzerland.

[‡]Rowland Institute at Harvard, 100 Edwin H. Land Blvd., Cambridge MA 02142, USA.

E-mail: eichlera@phys.ethz.ch

Abstract

We report spatially resolved measurements of static and fluctuating electric fields over conductive (Au) and non-conductive (SiO₂) surfaces. Using an ultrasensitive ‘nanoladder’ cantilever probe to scan over these surfaces at distances of a few tens of nanometers, we record changes in the probe resonance frequency and damping that we associate with static and fluctuating fields, respectively. We find that the two quantities are spatially correlated and of similar magnitude for the two materials. We quantitatively describe the observed effects on the basis of trapped surface charges and dielectric fluctuations in an adsorbate layer. Our results provide direct, spatial evidence for surface dissipation in adsorbates that affects nanomechanical sensors, trapped ions, superconducting resonators, and color centers in diamond.

Introduction – The last decades have seen rapid progress in the design and operation of devices for quantum applications. Today, we can build highly coherent qubits and resonators in optical, electrical and mechanical media, and interface these platforms with each other to create hybrid systems.^{1–6} Many important advances became possible through a reduction of the critical dimensions to the nanoscale, making the devices more sensitive, faster in their response, and more suitable for dense packaging. However, as dimensions are scaled down, devices become increasingly susceptible to the harmful influence of fluctuating microscopic degrees of freedom. The coherence of trapped ions^{7–11} and of superconducting Josephson circuits,^{12–14} for instance, is limited by fluctuating electrical fields. Evidence points to two-level systems in surface oxides and adsorbates as the microscopic origin of these fields.^{8,15–17} Similar surface effects could also explain the poorly understood non-contact

dissipation between closely spaced bodies that presents an obstacle for ultrasensitive scanning force microscopy.^{18–27} Fluctuating electric fields furthermore affect the coherence of Rydberg atoms,²⁸ color centers in diamond,^{29,30} and nanomechanical resonators.^{31,32}

In spite of the importance of understanding and overcoming these issues, the precise nature of the fluctuating fields is not sufficiently understood and remains the subject of an ongoing debate. This is largely due to experimental challenges. For instance, while atomic force microscopy (AFM) enables direct surface imaging, it usually lacks the sensitivity required to obtain conclusive evidence on non-contact dissipation beyond a few nanometers distance. Trapped ions, which are ideally suited for such investigations due to their high sensitivity, currently do not offer the imaging possibilities and nanoscale resolution of scanning probe methods.³³ For this reason, most previous studies relied on power laws of fluctuating forces or fields

as a function of temperature, frequency, or distance.^{18,21,24–27,34–40} Such studies, however, are difficult to interpret: on the one hand, a single model can produce different power laws at different distances¹⁰ or temperatures.^{39,40} On the other hand, various microscopic effects can combine to produce complex phenomena that thwart attempts at a simple explanation.¹⁶

In this work, we report direct, experimental evidence for the connection between surface dissipation and static variations in the surface potential. To this end, we employ a ‘nanoladder’ scanning force sensor that can detect force noise on the level of $1 \text{ aN}/\sqrt{\text{Hz}}$.⁴¹ This ultrasensitive probe allows us to produce scans of the non-contact dissipation a few tens of nm above surfaces. For comparison, we perform measurements over a metal (Au) and a dielectric (SiO_2). Over both substrates, we find that regions of high and low dissipation correlate with shifts of the mechanical resonance frequency that are attributed to ‘voltage patches’.^{42–47} We can reproduce our observations using an established model²³ for electrical field fluctuation in dielectrics together with basic assumptions.¹¹ Our study provides a key to the understanding of surface dissipation effects and a potential route for improving the coherence of many types of quantum devices.

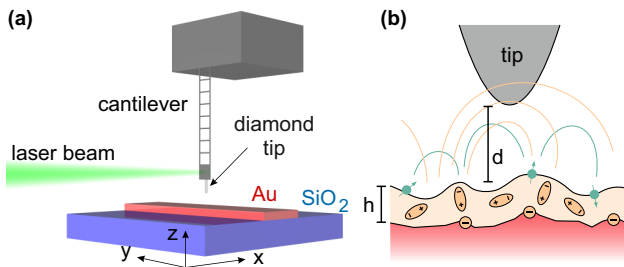


Figure 1: Experimental setup. (a) A nanoladder cantilever oscillates parallel to the surface in the x direction. It is scanned over a sample surface consisting of SiO_2 and a pattern of Au that is 250 nm thick and electrically grounded. (b) Schematic representation of the diamond tip interacting with electrical (magnetic) fields generated by charge (spin) defects close to the sample surface. A bright orange area indicates an adsorbant layer.

Device and setup. Our scanning force probe is a pendulum-style nanoladder cantilever made of single-crystal Si, see Fig. 1(a).⁴¹ The cantilever has a bare resonance frequency of $f_0 = 4.858 \text{ kHz}$, an effective mass of $m = 2.6 \text{ pg}$, and a quality factor of $Q_0 = 26100$, corresponding to a spring constant $k_0 = m4\pi^2 f_0^2 = 2.4 \text{ }\mu\text{N m}^{-1}$ and a damping coefficient $\Gamma_0 = m2\pi f_0/Q_0 = 3.1 \times 10^{-15} \text{ kg s}^{-1}$. To obtain a sharp, clean scanning tip, we attach a diamond nanowire^{48,49} to the end of the cantilever with a micro-manipulator. The displacement of the cantilever is detected by fiber-optical interferometry with a 1550 nm laser.^{41,50} Measurements are conducted in ultra-high vacuum at a temperature of about 4 K.

Experimental results – Our sample surface is a Si substrate with 1500 nm of thermally grown SiO_2 . A region of the surface is covered with a 250 nm-thick Au film by e-beam evaporation, see Fig. 1. We begin our investigations by recording maps of the cantilever frequency f at constant tip height, corresponding to the mean tip-surface distance d , see Fig. 2(a)-(b). The maps reveal distinct, reproducible variations in f on a length scale of 50 – 150 nm. Next, we perform linescans at different values of d and extract f and the quality factor Q from repeated ring-down measurements at every scan position, see Fig. 2(c)-(d). Data acquisition per point takes 100 – 300 s for this procedure. From these measurements, we can determine the coefficient of non-contact friction Γ_{NCF} as

$$\Gamma_{\text{NCF}} = \Gamma - \Gamma_0 = \frac{2\pi f m}{Q} - \frac{2\pi f_0 m}{Q_0}. \quad (1)$$

We observe significant variations of Γ_{NCF} at constant d over both materials, see Fig. 2(e)-(f). Further, the variations in Γ_{NCF} correlate with those of f ; maxima of f correspond to minima of Γ_{NCF} and vice versa. The variations smoothen out when increasing d . For $d \geq 100 \text{ nm}$, we retrieve the intrinsic damping of the cantilever, $\Gamma \approx \Gamma_0$.

Figure 3 summarizes the quantitative analysis of our data. First, we observe a general increase of the variations in both f and Γ_{NCF}

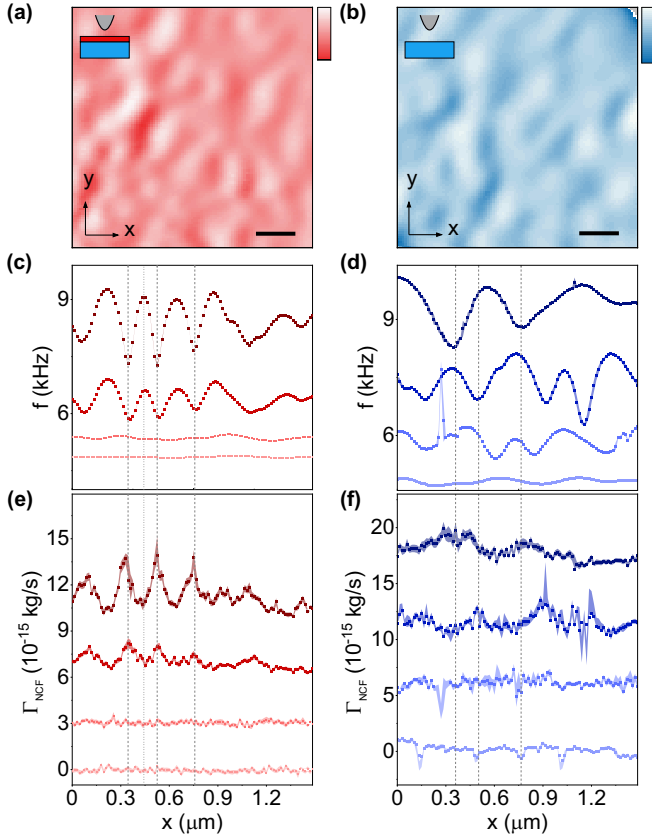


Figure 2: Scanning results. (a) Maps of the cantilever frequency f recorded at a distance $d = 30$ nm over Au and (b) $d = 80$ nm over SiO₂. The colors range from red (4500 Hz) to white (5000 Hz) in (a) and from blue (4200 Hz) to white (5210 Hz) in (b). Both scale bars are 100 nm long. Inserts show the tip over the substrate, SiO₂ (blue) and Au (red). (c)-(f) Line scans of the resonance frequency f and non-contact friction Γ_{NCF} over Au (c),(e) and SiO₂ (d),(f). The lines corresponds to $d = 150, 100, 45,$ and 30 nm for Au and $d = 100, 75, 60, 45$ nm for SiO₂ (bottom to top). Lines are offset for better visibility by 0, 0.5, 1.5, and 3.5 kHz in (c), 0, 1, 2.5, and 4.5 kHz in (d), 3×10^{-15} kg s⁻¹ each in (e) and 5×10^{-15} kg s⁻¹ each in (f). Shaded areas denote errors estimated from repeated measurements.

with decreasing d over both materials. Second, a strong increase of the mean value of Γ_{NCF} with decreasing d is detected. Third, a correlation between f and Γ_{NCF} is apparent close to the surface. These features are reproducible over surfaces of Au as well as SiO₂ at different positions over the sample, after thermal cycling

to room temperature, and with magnetic fields up to 4 T (cf. SI). The results clearly point to non-uniform electric fields generated in a surface layer that must be present without regard of the substrate material underneath. In the following, we discuss concrete models that can explain our measurements.

Model – When brought close to a material, the probe tip interacts with electrical or magnetic surface fields, cf. Fig. 1(b). In general, static fields are expected to modify the cantilever’s potential energy E_{pot} , and therefore the spring constant $k = \delta^2 E_{\text{pot}} / \delta x^2$ and the resonance frequency $f = \frac{1}{2\pi} \sqrt{k/m}$.⁵¹ Local variation of the electrical surface potential, dubbed ‘voltage patches’, were previously observed for various materials, and ascribed to trapped charges or work function differences for different crystalline facets.^{42–47} Irrespective of their microscopic origin, we model such voltage patches as isolated charges q_i trapped at the surface. For a point-like tip with a charge q_{tip} , shifts in f can be computed from the added electrostatic potential energy $E_{\text{el}} = \sum_i E_i$, where

$$E_i = \frac{1}{4\pi\epsilon_0} \frac{q_i q_{\text{tip}}}{r_i} \quad (2)$$

is the Coulomb energy of a surface charge q_i , with r_i the distance to the cantilever charge q_{tip} . With an electrostatic spring constant $k_{\text{el}} = \delta^2 E_{\text{el}} / \delta x^2$, we obtain

$$f = \frac{1}{2\pi} \sqrt{\frac{k_0}{m} + \frac{k_{\text{el}}}{m}} \approx f_0 + \frac{k_{\text{el}}}{8\pi^2 m f_0}, \quad (3)$$

where the last term is valid in the limit of $k_{\text{el}} \ll k_0$.

This simple electrostatic model can reproduce all main features of our frequency scans. The open dots in Fig. 3(a) show the maximum and minimum frequencies calculated for a square lattice of charges $q_i q_{\text{tip}} = 0.7 q_e^2$, where $q_e = 1.6 \times 10^{-19}$ C is the elementary charge and 0.7 is an arbitrary scaling factor chosen for best agreement with the experimental data. The model uses a site separation of 150 nm and an offset of $\Delta = 20$ nm between the tip apex

and the position of the effective charge to emulate the shape of the line scans in Fig. 2(c). The offset roughly corresponds to the expected tip apex radius, cf. SI for details. For SiO₂, the same model with $q_i q_{\text{tip}} = 1.6q_e^2$ yields best agreement with the experiment, see Fig. 3(b). The measured and simulated $f_{\text{min,max}}$ can be described by phenomenological power laws as described in the figure caption. The model is slightly asymmetric with respect to f_0 owing to the difference between the condition for negative f shifts (directly over a charge) and positive shifts (far from charges). This difference can be observed in the experiment as well, for instance for $d = 30$ nm in Fig. 2(c). The asymmetry appears to be weaker in the experimental data than in the model, which may be due to a spatial spread of the effective charges in the tip.

While static field gradients give rise to frequency shifts, dissipation is identified as a signature of fluctuating fields. Previous studies have addressed the role of fluctuating electrical or magnetic defects at surfaces for dissipation, both in the contexts of scanning force microscopy^{19–23,25–27} and, with a very similar framework, for trapped ions.^{7–11} These results established that electrical fluctuations intrinsic to the substrate, such as thermally excited currents or tip-induced mirror charges in a conductor, produce negligible effects under most circumstances.^{11,18–20} An alternative source of electrical fluctuations could be attributed to thin layers of adsorbants, such as hydrocarbons, that cover a surface immediately upon exposure to air.^{11,21,44,52} As our cryogenic system does not permit baking out of the sample chamber, we must assume such adsorbant layers to be present. The most basic model for understanding Γ_{NCF} , therefore, is based on thermal dielectric fluctuations in a thin layer covering the sample surfaces. We verified with additional measurements that the dominant contribution to Γ_{NCF} cannot be assigned to fluctuating surface electron spins, cf. SI.²⁵

We use the model derived in²³ to determine the value of Γ_{NCF} expected for a thin dielectric. For the adsorbate layer on Au, we use as typical values a relative permittivity $\epsilon = 2$ and a loss

tangent $\tan \theta = 0.01$.^{11,53} Defining the complex permittivity ϵ_c as

$$\epsilon_c = \epsilon(1 + i \tan \theta), \quad (4)$$

as well as the functions

$$\zeta = \frac{\epsilon_c - 1}{\epsilon_c + 1} \quad (5)$$

$$J_2 = \int_0^\infty \frac{(1 - e^{-4u(h/d)}) u^2 e^{-2u} du}{(1 + \zeta' e^{-2u(h/d)})^2 + (\zeta'' e^{-2u(h/d)})^2} \quad (6)$$

where ' and '' denote real and imaginary parts, respectively, the dissipation is calculated as²³

$$\Gamma_{\text{NCF}} = \frac{q_{\text{tip}}^2 \zeta''}{8\pi^2 \epsilon_0 f d^3} J_2 \quad (7)$$

with ϵ_0 being the permittivity of free space. Note that Eq. (7) describes the situation of a dielectric on a metal substrate, but we use it also to approximate the adsorbate layer on SiO₂. In the SI, we present a comparison to a second model that depicts the situation of two non-conducting layers and leads to very similar results.⁵⁴

Neither the effective tip charge q_{tip} nor its exact position in the diamond lattice is controlled in our experiment. The offset of $\Delta = 20$ nm between the tip apex and the charge position that we introduced for the electrostatic model is included for the dissipation calculations as well. From a rough experimental calibration of the effective tip charge, we get an upper bound of about $20q_e$ (cf. SI). However, the relevant number of charges must be significantly lower, because the calibration is sensitive to charges on distances of several μm , while our experiments only probe interactions on a scale of $d < 100$ nm, cf. Fig. 3(a)-(d). We obtain best results assuming $q_{\text{tip}} \approx q_e$.

There are several ways how Eq. (7) can be used to explain the experimentally observed variation in Γ_{NCF} . We start by noting that Eq. (7) has an explicit dependency $\Gamma_{\text{NCF}} \propto f^{-1}$, producing the correct trend seen in Fig. 2. However, the variation of Γ_{NCF} generated in this

way is too small to explain our experimental results, see dark shaded area in Fig. 3(c)-(d), suggesting that additional effects are taking place in parallel. For instance, it was previously found that the thickness of hydrocarbon layers on Au is typically between $h = 0.4$ nm (a monolayer) and 2.0 nm.^{11,55,56} Inserting such a variation in h into Eq. (7) yields a surprisingly close agreement with our measurements for Au, see Fig. 3(c). For SiO₂, the layer thickness required to reproduce our measurement for the given dielectric parameters is about 8 nm, which appears unrealistic. Instead, we present in Fig. 3(d) a model calculation with the same thickness variation as in (c), but with $\tan\theta = 0.03$. X-ray photoelectron spectroscopy measurements suggest that the chemical composition and bonding nature of the adventitious carbon on the two surfaces is indeed not identical (cf. SI). Considering the open questions regarding dielectric properties of nanometer-scale surface layers, the agreement that we find for both data sets is encouraging. Finally, we also obtain reasonable results when considering variations in d . For a thin dielectric layer ($h \ll d$), Eq. (7) yields approximately $\Gamma_{\text{NCF}} \propto d^{-4}$, resulting in dissipation variations due to sample topography. The surfaces investigated in this work, Au and SiO₂, show different surface roughness and grain size in AFM topographic scans (see SI). This differences make an interpretation of the f variations in Fig. 2(a)-(b) in terms of topographic features improbable. Finally, the expected Ohmic loss for bare Au¹¹ turns out to be about ten orders of magnitude smaller than the measured values of Γ_{NCF} , ruling out a contribution due to mirror charges in a conductor. In conclusion, it is likely that dielectric fluctuations in a thin surface layer are the dominant cause of non-contact friction in our system.

Discussion – We have set out to investigate the surface dissipation over different materials, selecting Au as a representative metal and SiO₂ as a dielectric. Our measurements provide evidence for a correlation between f and Γ_{NCF} over both substrates despite their different electronic properties. The plots in Figs. 3(e)-(f) suggest $\Gamma_{\text{NCF}} \propto f^{-1}$, even though the explicit

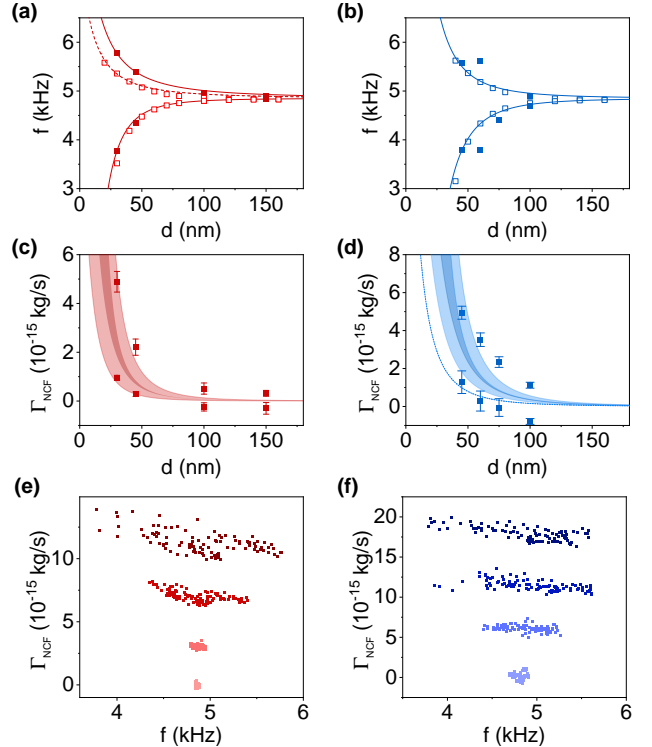


Figure 3: Quantitative data analysis. (a) Maximum and minimum f as a function of d over Au and (b) over SiO₂. Filled and open squares correspond to our measurements and to model calculations, respectively. Solid lines are phenomenological fits using $f_0 \pm \beta_{\pm}/(d + \Delta)^{\nu_{\pm}}$. For Au, $\beta_- = 3 \times 10^{-23}$ Hz m^{3.5} and $\nu_- = 3.5$, $\beta_+ = 2.3 \times 10^{-12}$ Hz m² and $\nu_+ = 2$ ($\beta_+ = 1.25 \times 10^{-12}$ Hz m² for the dashed line). For SiO₂, $\beta_- = 7.5 \times 10^{-23}$ Hz m^{3.5} and $\nu_- = 3.5$, $\beta_+ = 1.8 \times 10^{-19}$ Hz m³ and $\nu_+ = 3$. See main text and SI for details on the model. (c) Measured Γ_{NCF} and corresponding model for Au and (d) for SiO₂. Squares indicate the maxima and minima of a linescan at a distance d . The shaded areas corresponds to the model predictions for varying f [cf. solid lines in (a)-(b)] for $h = 1.0$ nm (dark shade) and for h between 0.4 and 2.0 nm (bright shade). We use $q_{\text{tip}} = q_e$ for both models, $\epsilon = 2$ and $\tan\theta = 0.01$ for Au, and $\epsilon = 2$ and $\tan\theta = 0.03$ for SiO₂. The dashed line in (d) is the additive dielectric contribution of the SiO₂ substrate with a thickness of 1.5 μm , $\epsilon = 4.44$ and $\tan\theta = 10^{-3}$. (e) Measured Γ_{NCF} as function of f for different d as in Fig. 2 over Au and (f) over SiO₂. Data sets are offset for better visibility by 2×10^{-15} kg s⁻¹ each.

f^{-1} dependency in Eq. (7), in concert with the measured variations in f , is not sufficient to explain the experimentally observed variations in Γ_{NCF} . We propose a simple model where minima (maxima) of f coincide either with maxima (minima) of h or with minima (maxima) of d . The microscopic mechanisms behind such correlations are at present speculative, but appear to originate from the electrostatic voltage patches close to the surface. For instance, surface potential patches exert attractive forces onto molecules with a dipole moment, which can lead to site-selective adsorption⁴⁴ and a maximum of h directly over static charges. Alternatively, a correlation between topographic features (d) and static charges is to be expected if the voltage patches are generated by differences in the surface work function at crystallographic grain orientations, as proposed in Ref.⁴⁶

With a tip charge estimated as $q_{\text{tip}} = q_e$, we can quantify the power spectral density of the fluctuating electrical field as

$$S_E = 4k_B T \Gamma_{\text{NCF}} / q_e^2. \quad (8)$$

The values we obtain from Eq. (8) are in the range of $10 - 100 \text{ V}^2 \text{ m}^{-2} \text{ Hz}^{-1}$, which is $10^{11} - 10^{15}$ times larger than what is typically detected with trapped ions.¹⁰ This discrepancy is not surprising, because the distance to the surface d in our measurements is about $10^3 - 10^4$ times smaller than in an ion-trap experiment. With the phenomenological power law $\Gamma_{\text{NCF}} \propto d^{-4}$ that we obtained in the thin-film limit from Eq. (7), we should expect a difference by a factor $10^{12} - 10^{16}$.

It is worth comparing our work to previous studies of fluctuating electrical fields with nanomechanical sensors in the $d = 10 - 100 \text{ nm}$ range.^{18,21,34} We note that those studies concentrated mostly on the d^{-n} dependence at single points over a sample. The values of n that were found varied strongly, from $1 < n < 1.5$ in Ref.¹⁸ to $n \geq 3$ in Ref.³⁴ Our experimental data are in rough agreement with the exponent $n \approx 4$ predicted for thin dielectric layers.^{21,23} Furthermore, our study also investigates the spatial pattern of Γ_{NCF} . The significant variations we

find on a 100 nm scale, over conducting and dielectric surfaces alike, offer a potential explanation for the apparent discrepancies in earlier results. In addition, we clearly demonstrate that Γ_{NCF} is connected to electrostatic interactions.

Conclusion and outlook – Based on our experimental data and on the agreement with theory, we identify surface adsorbants as the likely origin of non-contact friction over conducting and insulating materials. This result resolves much of the previous disagreement between experiments and models – even over superconducting surfaces, such thin dielectric layers are often unavoidable. (A notable exception is the experiment from Kisiel et al.²⁴ that was conducted after baking out the vacuum chamber.) A second finding is that fluctuating fields vary spatially and in concert with static surface potentials. This finding provides an important clue to the formation of adsorbants and, potentially, a strategy to reduce their impact. Such a strategy would benefit many of the most advanced fields in quantum sensing and quantum computation, in particular trapped ions, superconducting qubits and ultrasensitive force probes.^{4,10,11,14,57}

In order to reduce S_E and Γ_{NCF} , future work should focus on the microscopic connection between adsorbants and surface potentials. Nanomechanical probes can be complemented with nuclear magnetic resonance pulses to elucidate the chemical composition of surface layers.⁵⁷⁻⁵⁹ Other scanning tools like nanoscale SQUIDS^{60,61} or diamond probes with optically active nitrogen-vacancy defects⁶²⁻⁶⁴ could also play a crucial role in the quest to understand and overcome the influence of surface impurities. Finally, directed chemical functionalization with molecular monolayers that feature tailored electronic properties, i.e., defect-tolerant and long-range dipole alignment,⁶⁵ may be explored to mitigate fluctuating electric fields at the interface.

Acknowledgement We gratefully acknowledge discussions with Jonathan Home, Thomas Ihn, Marc-Dominik Krass, Roger Loring, John

Marohn, Clemens Müller, and Oded Zilberberg, the MRFM team of the Degen group, as well as technical support by U. Grob and P. Märki. This work is supported by the Swiss National Science Foundation (SNSF) through the Sinergia Project ZEPTO, Grant No. CRSII5.177198/1, the National Center of Competence in Research in Quantum Science and Technology, an ETH Research Grant ETH-03 16-1, and the FIRST cleanroom facility at ETH. Ye Tao is supported by a Rowland Fellowship.

References

- (1) Duan, L.-M.; Monroe, C. Colloquium: Quantum networks with trapped ions. *Rev. Mod. Phys.* **2010**, *82*, 1209–1224.
- (2) Xiang, Z.-L.; Ashhab, S.; You, J. Q.; Nori, F. Hybrid quantum circuits: Superconducting circuits interacting with other quantum systems. *Rev. Mod. Phys.* **2013**, *85*, 623–653.
- (3) Aspelmeyer, M.; Kippenberg, T. J.; Marquardt, F. Cavity optomechanics. *Rev. Mod. Phys.* **2014**, *86*, 1391–1452.
- (4) Degen, C. L.; Reinhard, F.; Cappellaro, P. Quantum sensing. *Rev. Mod. Phys.* **2017**, *89*, 035002.
- (5) Bruzewicz, C. D.; Chiaverini, J.; McConnell, R.; Sage, J. M. Trapped-ion quantum computing: Progress and challenges. *Applied Physics Reviews* **2019**, *6*, 021314.
- (6) Kjaergaard, M.; Schwartz, M. E.; Braumüller, J.; Krantz, P.; Wang, J. I.-J.; Gustavsson, S.; Oliver, W. D. Superconducting qubits: Current state of play. *Annual Review of Condensed Matter Physics* **2020**, *11*, 369–395.
- (7) Turchette, Q. A.; Kielpinski, King, B. E.; Leibfried, D.; Meekhof, D. M.; Myatt, C. J.; Rowe, M. A.; Sackett, C. A.; Wood, C. S.; Itano, W. M.; Monroe, C.; Wineland, D. J. Heating of trapped ions from the quantum ground state. *Physical Review A* **2000**, *61*, 063418, Publisher: American Physical Society.
- (8) Labaziewicz, J.; Ge, Y.; Leibbrandt, D. R.; Wang, S. X.; Shewmon, R.; Chuang, I. L. Temperature Dependence of Electric Field Noise above Gold Surfaces. *Physical Review Letters* **2008**, *101*, 180602.
- (9) Safavi-Naini, A.; Rabl, P.; Weck, P. F.; Sadeghpour, H. R. Microscopic model of electric-field-noise heating in ion traps. *Physical Review A* **2011**, *84*, 023412, Publisher: American Physical Society.
- (10) Brownnutt, M.; Kumph, M.; Rabl, P.; Blatt, R. Ion-trap measurements of electric-field noise near surfaces. *Reviews of Modern Physics* **2015**, *87*, 1419–1482, Publisher: American Physical Society.
- (11) Kumph, M.; Henkel, C.; Rabl, P.; Brownnutt, M.; Blatt, R. Electric-field noise above a thin dielectric layer on metal electrodes. *New Journal of Physics* **2016**, *18*, 023020, Publisher: IOP Publishing.
- (12) Gao, J.; Daal, M.; Vayonakis, A.; Kumar, S.; Zmuidzinas, J.; Sadoulet, B.; Mazin, B. A.; Day, P. K.; Leduc, H. G. Experimental evidence for a surface distribution of two-level systems in superconducting lithographed microwave resonators. *Applied Physics Letters* **2008**, *92*, 152505.
- (13) Wang, H.; Hofheinz, M.; Wenner, J.; Ansmann, M.; Bialczak, R. C.; Lenander, M.; Lucero, E.; Neeley, M.; O’Connell, A. D.; Sank, D.; Weides, M.; Cleland, A. N.; Martinis, J. M. Improving the coherence time of superconducting coplanar resonators. *Applied Physics Letters* **2009**, *95*, 233508.
- (14) Müller, C.; Cole, J. H.; Lisenfeld, J. Towards understanding two-level-systems in amorphous solids: insights from quantum circuits. *Reports on Progress in Physics*

- 2019**, *82*, 124501, Publisher: IOP Publishing.
- (15) Allcock, D.; Guidoni, L.; Harty, T.; Balance, C.; Blain, M.; Steane, A.; Lucas, D. Reduction of heating rate in a microfabricated ion trap by pulsed-laser cleaning. *New Journal of Physics* **2011**, *13*, 123023.
- (16) Hite, D. A.; Colombe, Y.; Wilson, A. C.; Brown, K. R.; Warring, U.; Jördens, R.; Jost, J. D.; McKay, K. S.; Pappas, D. P.; Leibfried, D.; Wineland, D. J. 100-Fold Reduction of Electric-Field Noise in an Ion Trap Cleaned with In Situ Argon-Ion-Beam Bombardment. *Physical Review Letters* **2012**, *109*, 103001, Publisher: American Physical Society.
- (17) Safavi-Naini, A.; Kim, E.; Weck, P. F.; Rabl, P.; Sadeghpour, H. R. Influence of monolayer contamination on electric-field-noise heating in ion traps. *Physical Review A* **2013**, *87*, 023421, Publisher: American Physical Society.
- (18) Stipe, B. C.; Mamin, H. J.; Stowe, T. D.; Kenny, T. W.; Rugar, D. Noncontact Friction and Force Fluctuations between Closely Spaced Bodies. *Physical Review Letters* **2001**, *87*, 096801, Publisher: American Physical Society.
- (19) Volokitin, A. I.; Persson, B. N. J. Noncontact friction between nanostructures. *Physical Review B* **2003**, *68*, 155420.
- (20) Zurita-Sánchez, J. R.; Greffet, J.-J.; Novotny, L. Friction forces arising from fluctuating thermal fields. *Physical Review A* **2004**, *69*, 022902, Publisher: American Physical Society.
- (21) Kuehn, S.; Loring, R. F.; Marohn, J. A. Dielectric Fluctuations and the Origins of Noncontact Friction. *Physical Review Letters* **2006**, *96*, 156103, Publisher: American Physical Society.
- (22) Volokitin, A. I.; Persson, B. N. J. Near-field radiative heat transfer and noncontact friction. *Reviews of Modern Physics* **2007**, *79*, 1291–1329.
- (23) Yazdaniyan, S. M.; Marohn, J. A.; Loring, R. F. Dielectric fluctuations in force microscopy: Noncontact friction and frequency jitter. *The Journal of Chemical Physics* **2008**, *128*.
- (24) Kisiel, M.; Gnecco, E.; Gysin, U.; Marot, L.; Rast, S.; Meyer, E. Suppression of electronic friction on Nb films in the superconducting state. *Nature Materials* **2011**, *10*, 119–122, Number: 2 Publisher: Nature Publishing Group.
- (25) She, J.-H.; Balatsky, A. V. Noncontact Friction and Relaxational Dynamics of Surface Defects. *Physical Review Letters* **2012**, *108*, 136101, Publisher: American Physical Society.
- (26) den Haan, A. M. J.; Wagenaar, J. J. T.; de Voogd, J. M.; Koning, G.; Oosterkamp, T. H. Spin-mediated dissipation and frequency shifts of a cantilever at milliKelvin temperatures. *Physical Review B* **2015**, *92*, 235441, Publisher: American Physical Society.
- (27) de Voogd, J. M.; Wagenaar, J. J. T.; Oosterkamp, T. H. Dissipation and resonance frequency shift of a resonator magnetically coupled to a semiclassical spin. *Scientific Reports* **2017**, *7*, 42239, Number: 1 Publisher: Nature Publishing Group.
- (28) Carter, J. D.; Martin, J. D. D. Coherent manipulation of cold Rydberg atoms near the surface of an atom chip. *Phys. Rev. A* **2013**, *88*, 043429.
- (29) Kim, M.; Mamin, H. J.; Sherwood, M. H.; Ohno, K.; Awschalom, D. D.; Rugar, D. Decoherence of Near-Surface Nitrogen-Vacancy Centers Due to Electric Field Noise. *Phys. Rev. Lett.* **2015**, *115*, 087602.
- (30) Jamonneau, P.; Lesik, M.; Tétienne, J. P.; Alvizu, I.; Mayer, L.; Dréau, A.; Kosen, S.; Roch, J.-F.; Pezzagna, S.; Meijer, J.; Teraji, T.; Kubo, Y.; Bertet, P.; Maze, J. R.;

- Jacques, V. Competition between electric field and magnetic field noise in the decoherence of a single spin in diamond. *Phys. Rev. B* **2016**, *93*, 024305.
- (31) Tao, Y.; Navaretti, P.; Hauert, R.; Grob, U.; Poggio, M.; Degen, C. L. Permanent reduction of dissipation in nanomechanical Si resonators by chemical surface protection. *Nanotechnology* **2015**, *26*, 465501.
- (32) Hamoumi, M.; Allain, P. E.; Hease, W.; Gil-Santos, E.; Morgenroth, L.; Gérard, B.; Lemaître, A.; Leo, G.; Favero, I. Microscopic Nanomechanical Dissipation in Gallium Arsenide Resonators. *Phys. Rev. Lett.* **2018**, *120*, 223601.
- (33) Maiwald, R.; Leibfried, D.; Britton, J.; Bergquist, J. C.; Leuchs, G.; Wineland, D. J. Stylus ion trap for enhanced access and sensing. *Nature Physics* **2009**, *5*, 551–554.
- (34) Gotsmann, B.; Fuchs, H. Dynamic Force Spectroscopy of Conservative and Dissipative Forces in an Al-Au(111) Tip-Sample System. *Physical Review Letters* **2001**, *86*, 2597–2600, Publisher: American Physical Society.
- (35) Yazdanian, S. M.; Hoepker, N.; Kuehn, S.; Loring, R. F.; Marohn, J. A. Quantifying Electric Field Gradient Fluctuations over Polymers Using Ultrasensitive Cantilevers. *Nano Letters* **2009**, *9*, 2273–2279, Publisher: American Chemical Society.
- (36) Saitoh, K.; Hayashi, K.; Shibayama, Y.; Shirahama, K. Gigantic Maximum of Nanoscale Noncontact Friction. *Physical Review Letters* **2010**, *105*, 236103, Publisher: American Physical Society.
- (37) Chiaverini, J.; Sage, J. M. Insensitivity of the rate of ion motional heating to trap-electrode material over a large temperature range. *Phys. Rev. A* **2014**, *89*, 012318.
- (38) Bruzewicz, C. D.; Sage, J. M.; Chiaverini, J. Measurement of ion motional heating rates over a range of trap frequencies and temperatures. *Phys. Rev. A* **2015**, *91*, 041402.
- (39) Sedlacek, J. A.; Stuart, J.; Slichter, D. H.; Bruzewicz, C. D.; McConnell, R.; Sage, J. M.; Chiaverini, J. Evidence for multiple mechanisms underlying surface electric-field noise in ion traps. *Physical Review A* **2018**, *98*, 063430, Publisher: American Physical Society.
- (40) Noel, C.; Berlin-Udi, M.; Matthiesen, C.; Yu, J.; Zhou, Y.; Lordi, V.; Häffner, H. Electric-field noise from thermally activated fluctuators in a surface ion trap. *Physical Review A* **2019**, *99*, 063427, Publisher: American Physical Society.
- (41) Héritier, M.; Eichler, A.; Pan, Y.; Grob, U.; Shorubalko, I.; Krass, M. D.; Tao, Y.; Degen, C. L. Nanoladder Cantilevers Made from Diamond and Silicon. *Nano Lett.* **2018**, *18*, 1814–1818.
- (42) Camp, J. B.; Darling, T. W.; Brown, R. E. Macroscopic variations of surface potentials of conductors. *Journal of Applied Physics* **1991**, *69*, 7126–7129.
- (43) Burnham, N. A.; Colton, R. J.; Pollock, H. M. Work-function anisotropies as an origin of long-range surface forces. *Physical Review Letters* **1992**, *69*, 144–147, Publisher: American Physical Society.
- (44) Rossi, F.; Opat, G. I. Observations of the effects of adsorbates on patch potentials. *Journal of Physics D: Applied Physics* **1992**, *25*, 1349–1353, Publisher: IOP Publishing.
- (45) Speake, C. C.; Trenkel, C. Forces between Conducting Surfaces due to Spatial Variations of Surface Potential. *Physical Review Letters* **2003**, *90*, 160403.

- (46) Gaillard, N.; Gros-Jean, M.; Mariolle, D.; Bertin, F.; Bsiesy, A. Method to assess the grain crystallographic orientation with a submicronic spatial resolution using Kelvin probe force microscope. *Applied Physics Letters* **2006**, *89*, 154101, Publisher: American Institute of Physics.
- (47) Robertson, N. A.; Blackwood, J. R.; Buchman, S.; Byer, R. L.; Camp, J.; Gill, D.; Hanson, J.; Williams, S.; Zhou, P. Kelvin probe measurements: investigations of the patch effect with applications to ST-7 and LISA. *Classical and Quantum Gravity* **2006**, *23*, 2665–2680.
- (48) Tao, Y.; Degen, C. L. Single-Crystal Diamond Nanowire Tips for Ultrasensitive Force Microscopy. *Nano Letters* **2015**, *15*, 7893–7897.
- (49) Tao, Y.; Eichler, A.; Holzherr, T.; Degen, C. L. Ultrasensitive mechanical detection of magnetic moment using a commercial disk drive write head. *Nature Communications* **2016**, *7*, 1–8.
- (50) Rugar, D.; Mamin, H.; Guethner, P. Improved fiber-optic interferometer for atomic force microscopy. *Applied Physics Letters* **1989**, *55*, 2588–2590.
- (51) Kozinsky, I.; Postma, H. C.; Bargatin, I.; Roukes, M. Tuning nonlinearity, dynamic range, and frequency of nanomechanical resonators. *Applied Physics Letters* **2006**, *88*, 253101.
- (52) Smith, T. The hydrophilic nature of a clean gold surface. *Journal of Colloid and Interface Science* **1980**, *75*, 51–55.
- (53) Kaye, G. W. C.; Laby, T. H. *Tables of Physical and Chemical Constants*; Longman: Harlow, England, UK, 1995.
- (54) Lekkala, S.; Marohn, J. A.; Loring, R. F. Electric force microscopy of semiconductors: Theory of cantilever frequency fluctuations and noncontact friction. *The Journal of Chemical Physics* **2013**, *139*, 184702.
- (55) Degen, C.; Poggio, M.; Mamin, H.; Rettnner, C.; Rugar, D. Nanoscale magnetic resonance imaging. *Proceedings of the National Academy of Sciences* **2009**, *106*, 1313–1317.
- (56) Loretz, M.; Pezzagna, S.; Meijer, J.; Degen, C. Nanoscale nuclear magnetic resonance with a 1.9-nm-deep nitrogen-vacancy sensor. *Applied Physics Letters* **2014**, *104*, 033102.
- (57) Poggio, M.; Degen, C. L. Force-detected nuclear magnetic resonance: recent advances and future challenges. *Nanotechnology* **2010**, *21*, 342001.
- (58) Rose, W.; Haas, H.; Chen, A. Q.; Jeon, N.; Lauhon, L. J.; Cory, D. G.; Budakian, R. High-resolution nanoscale solid-state nuclear magnetic resonance spectroscopy. *Physical Review X* **2018**, *8*, 011030.
- (59) Grob, U.; Krass, M. D.; Héritier, M.; Pachlatko, R.; Rhensius, J.; Košata, J.; Moores, B. A.; Takahashi, H.; Eichler, A.; Degen, C. L. Magnetic Resonance Force Microscopy with a One-Dimensional Resolution of 0.9 Nanometers. *Nano Letters* **2019**, *19*, 7935–7940.
- (60) Finkler, A.; Segev, Y.; Myasoedov, Y.; Rappaport, M. L.; Ne’eman, L.; Vasyukov, D.; Zeldov, E.; Huber, M. E.; Martin, J.; Yacoby, A. Self-aligned nanoscale SQUID on a tip. *Nano Letters* **2010**, *10*, 1046–1049.
- (61) Vasyukov, D.; Ceccarelli, L.; Wyss, M.; Gross, B.; Schwarb, A.; Mehlin, A.; Rossi, N.; Tütüncüoğlu, G.; Heimbach, F.; Zamani, R.; Kovács, A.; Fontcuberta i Morral, A.; Grundler, D.; Poggio, M. Imaging stray magnetic field of individual ferromagnetic nanotubes. *Nano Letters* **2018**, *18*, 964–970.
- (62) Degen, C. Scanning magnetic field microscope with a diamond single-spin sensor. *Applied Physics Letters* **2008**, *92*, 243111.

- (63) Maze, J.; Stanwix, P.; Hodges, J.; Hong, S.; Taylor, J.; Cappellaro, P.; Jiang, L.; Dutt, M. G.; Togan, E.; Zibrov, A.; Yacoby, A.; Walsworth, R. L.; Lukin, M. D. Nanoscale magnetic sensing with an individual electronic spin in diamond. *Nature* **2008**, *455*, 644.
- (64) Balasubramanian, G.; Chan, I.; Kolesov, R.; Al-Hmoud, M.; Tisler, J.; Shin, C.; Kim, C.; Wojcik, A.; Hemmer, P. R.; Krueger, A.; Hanke, T.; Leitenstorfer, A.; Bratschitsch, R.; Jelezko, F.; Wrachtrup, J. Nanoscale imaging magnetometry with diamond spins under ambient conditions. *Nature* **2008**, *455*, 648.
- (65) Thomas, J.; Schwartz, J.; Hohman, J.; Claridge, S.; Auluck, H.; Serino, A.; Spokoyny, A.; Tran, G.; Kelly, K.; Mirkin, C.; Gilles, J.; Osher, S.; Weiss, P. Defect-tolerant aligned dipoles within two-dimensional plastic lattices. *ACS Nano* **2015**, *9*, 4734–4742.

Supplementary Material: Spatially resolved surface dissipation over metal and dielectric substrates

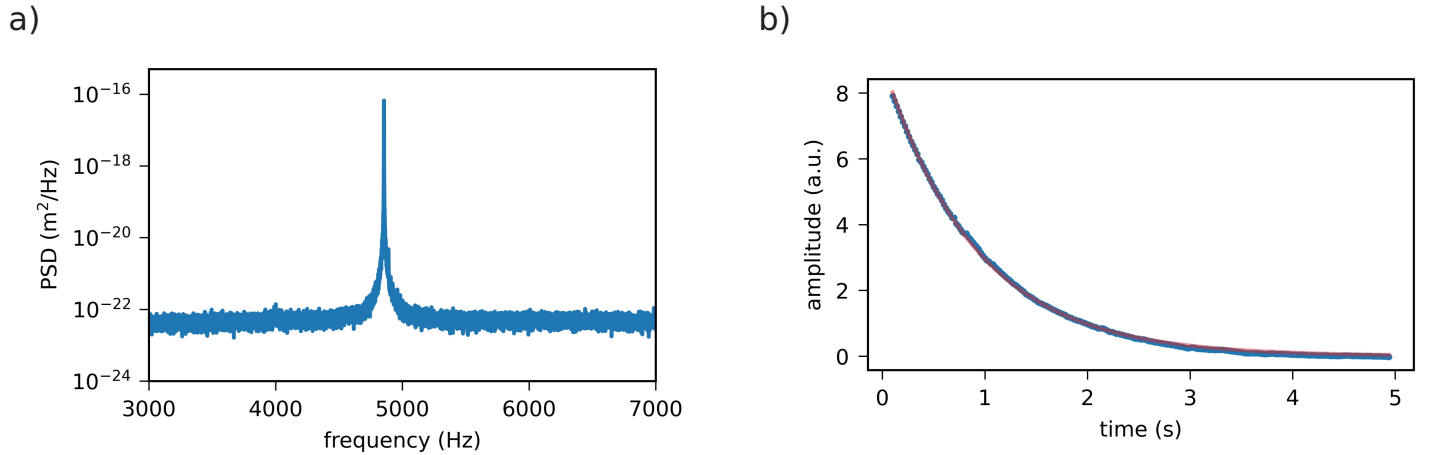
Martin Hérítier[†], Raphael Pachlatko[†], Ye Tao[‡], John M. Abendroth[†], Christian L. Degen[†], and Alexander Eichler[†]

[†]Laboratory for Solid State Physics, ETH Zürich, CH-8093 Zürich, Switzerland.

[‡]Rowland Institute at Harvard, 100 Edwin H. Land Blvd., Cambridge MA 02142, USA

Cantilever characterization

Details about the silicon nanoladder cantilever design were reported in a previous publication.^{S1} In Fig. S1(a), we show the displacement power spectral density (PSD), measured at 4 K, of the cantilever used in this study. We use such measurements at room temperature to calibrate the effective resonator mass m , and repeat them at cryogenic temperatures to verify the effective temperature T of the sensor. A typical ringdown experiment used to determine the Q -factor is displayed in Fig. S1(b).



Supplementary Figure S1: (a) Cantilever displacement power spectral density around its fundamental frequency of 4.858 kHz at 4 K. (b) Typical cantilever ringdown measurement. The decay of the amplitude is averaged over 10 – 20 runs and fitted by an exponential decay (red line).

Model of two dielectric layers

In the main text, we use the model by Yazdanian et al. to calculate the non-contact friction due to dielectric fluctuations in thin adsorbant layers on Au and SiO₂.^{S2} The model assumes that the dielectric layer is directly supported by a metal, as is the case for our Au sample. For SiO₂, the situation is slightly different, as the adsorbant layer is supported by a second dielectric (SiO₂) whose influence we account for by an additive term in Γ_{NCF} that we calculate with the same equation, see dashed line in Fig. 3(c). We neglect the influence of the Si substrate that is more than 1 μm away from the tip.

A more rigorous way to calculate Γ_{NCF} for our SiO_2 sample is provided by the model by Lekkala et al.^{S3} In this model, a dielectric and a semiconducting layer are considered. By setting the density of free charges in the semiconductor to be zero, we arrive at a model for two dielectric layers.

The equation to calculate Γ_{NCF} with the Lekkala model is^{S3}

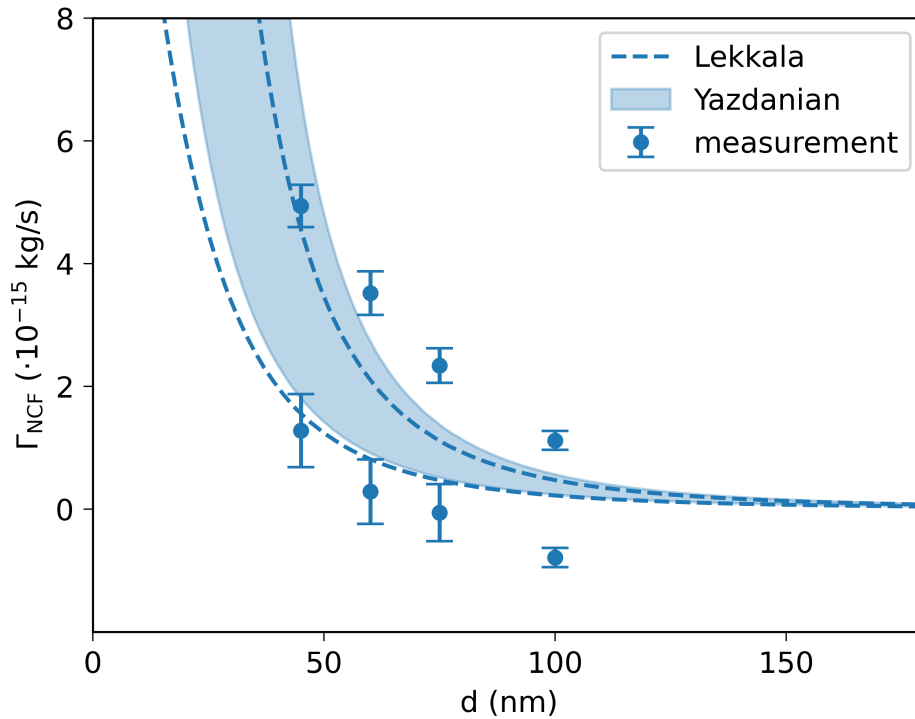
$$\Gamma_{\text{NCF}} = -\frac{q_{\text{tip}}^2}{16\pi^2 f \epsilon_0} \int_0^\infty du u^2 e^{-2ud} \text{Im} \left(\frac{\epsilon_c - \xi(u)}{\epsilon_c + \xi(u)} \right) \quad (\text{S1})$$

Here, we use the definitions

$$\xi(u) = \frac{\sinh(uh)^2 + \alpha \cosh(uh) \sinh(uh)}{\alpha \sinh(uh)^2 + \cosh(uh) \sinh(uh)}, \quad (\text{S2})$$

$$\alpha = \frac{\epsilon_c}{\epsilon_{\text{SiO}_2}}, \quad (\text{S3})$$

where ϵ_{SiO_2} is the relative dielectric permittivity of the SiO_2 substrate and all other parameters are defined as in the main text. The results we obtain with this model, using identical values as in the main text, are shown in Fig. S2. We find a small quantitative difference compared to the Yazdanian model.



Supplementary Figure S2: Comparison of the results for Γ_{NCF} of a dielectric layer with $\epsilon = 2$, $\tan \theta = 0.03$ and $0.4 < h < 2$ nm, over a $1.5 \mu\text{m}$ -thick layer of SiO_2 , calculated with the models by Yazdanian et al.^{S2} and Lekkala et al.^{S3}

Results with magnetic field

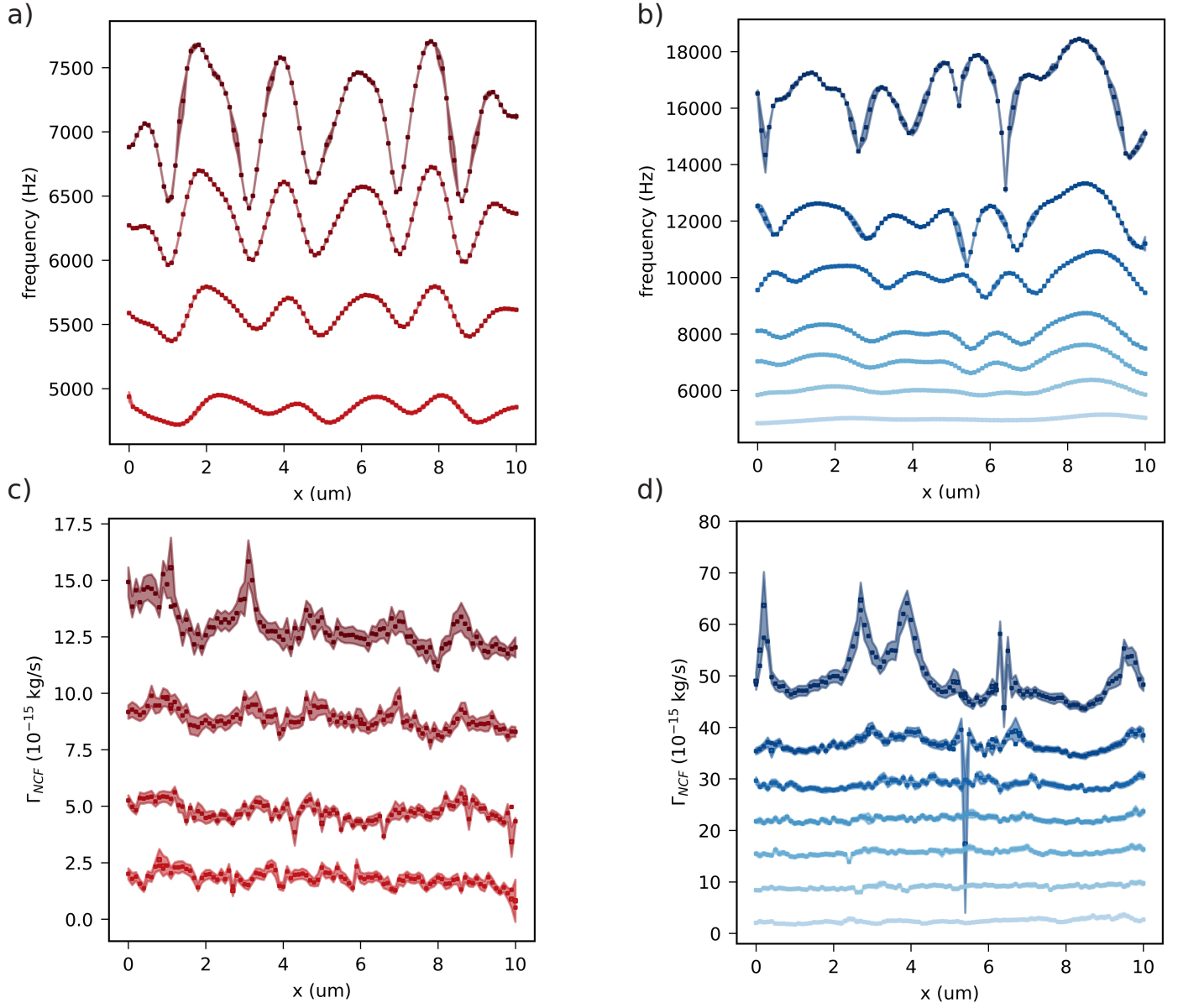
In this section, we present the data measured under an external magnetic field of $B = 4$ T applied in the z -direction. At this field, the Boltzmann energy $k_{\text{B}}T$ and the magnetic potential energy

$\mu_B H$ of electron spins are approximately equal, where $k_B = 1.38 \times 10^{-23} \text{ J K}^{-1}$ is the Boltzmann constant, $T = 4 \text{ K}$ is the temperature, and $\mu_B = 9.3 \times 10^{-24} \text{ J T}^{-1}$ is the Bohr magneton. We would therefore expect a noticeable change in Γ_{NCF} if fluctuating electronic spins are responsible for it.

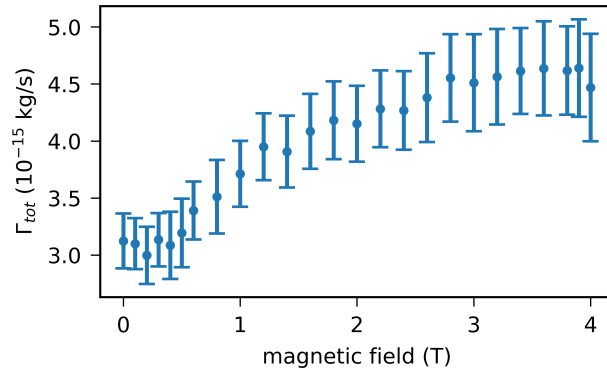
In Fig. S3, we show the line scans of frequency f and non-contact friction Γ_{NCF} as in Fig. 2 of the main paper. Figure S4(a) displays the dependency of the total cantilever dissipation Γ_{tot} on the external magnetic field far from the surface. We see that the cantilever damping increases with B , potentially due to magnetic impurities on the cantilever surface.

To test the surface dissipation added by the presence of the magnetic field, we extract the maxima and minima of the line scans of Γ_{NCF} in Fig. S3(c)-(d) and plot them versus d , see Fig. S5. For both materials, the data points agree with those for $B = 0$ within the expected statistical spread. From these findings, we conclude that the dominant contribution to Γ_{NCF} over both materials must be assigned to electrical fluctuations that are independent of B .

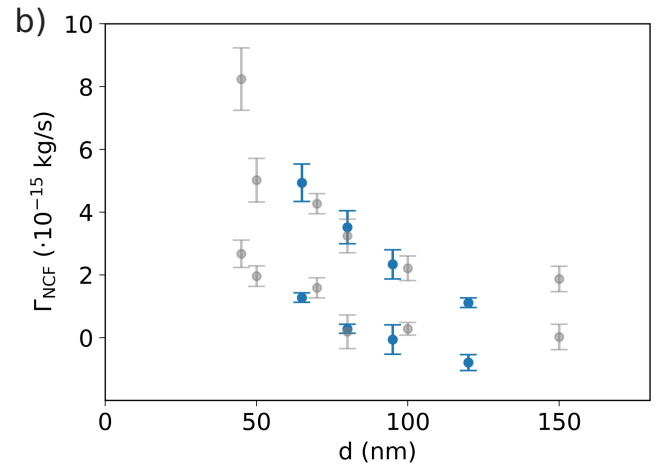
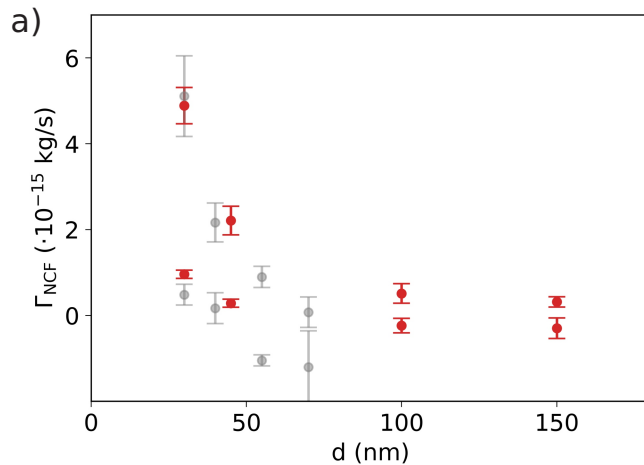
Finally, we show in Fig. S6 the complementary plots to fig. 3(e)-(f) of the main text. As for $B = 0$, a clear correlation between Γ_{NCF} and f is apparent.



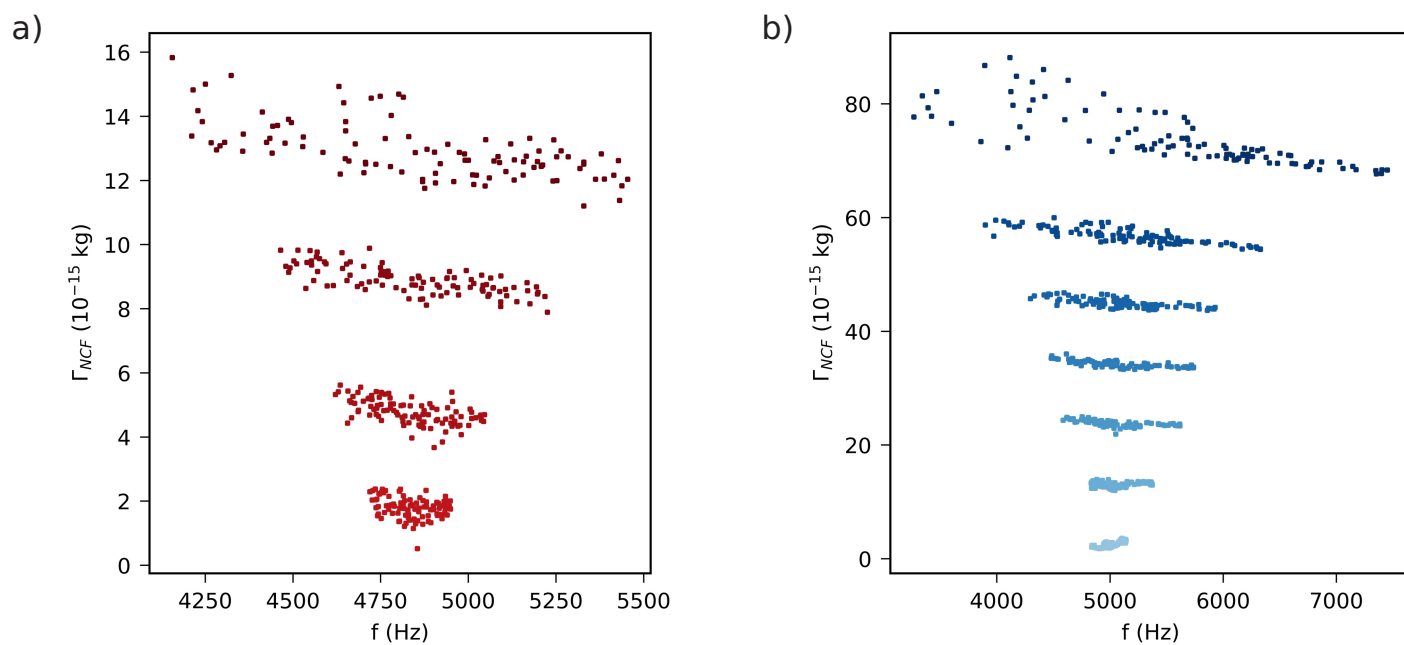
Supplementary Figure S3: Line scans of the resonance frequency f and non-contact friction Γ_{NCF} over Au (a)-(c) and SiO_2 (b)-(d) under an external magnetic field of 4 T for $d = 20, 30, 45, 60$ nm over Au and $d = 30, 45, 50, 70, 80, 100, 150$ nm over SiO_2 (top to bottom). Lines are offset for better visibility by 0.075 kHz each in (a), 11, 7, 5, 3, 2, 1 kHz in (b), 3×10^{-15} kg s $^{-1}$ each in (c), and 6×10^{-15} kg s $^{-1}$ each in (d).



Supplementary Figure S4: Dissipation Γ_{tot} as function of magnetic field far from the surface.



Supplementary Figure S5: Maximum and minimum measured Γ_{NCF} under an external magnetic field of 4 T (grey data points). For comparison, the measured values without external field from Fig. 3 of the main manuscript are also shown (red, blue).



Supplementary Figure S6: Γ_{NCF} as function of f in the presence of an external magnetic field of 4 T over Au (a) and over SiO_2 (b). Data are offset for better visibility by $3 \times 10^{-15} \text{ kg s}^{-1}$ each in (a), and $10 \times 10^{-15} \text{ kg s}^{-1}$ each in (b).

Charge calibration

This section presents our calibration procedure to estimate the charge q_{tip} carried by the cantilever tip. We take advantage of the fact that our sample is a stripline used for inverting spins in magnetic resonance experiments.^{S4} We apply a voltage to that stripline to electrostatically drive the cantilever vibrations. We then determine the force via the cantilever response function:

$$A(\omega) = \frac{F_d/m}{\sqrt{(\omega_0^2 - \omega^2)^2 + \left(\frac{\omega_0\omega}{Q}\right)^2}} \quad (\text{S4})$$

where $A(\omega)$ is the cantilever amplitude, F_d is the drive force, m and Q the cantilever's effective mass and quality factor, $\omega_0/2\pi = f_0$ its resonance frequency, and $\omega/2\pi$ the drive frequency. Measuring the amplitude at resonance, the force is therefore given by:

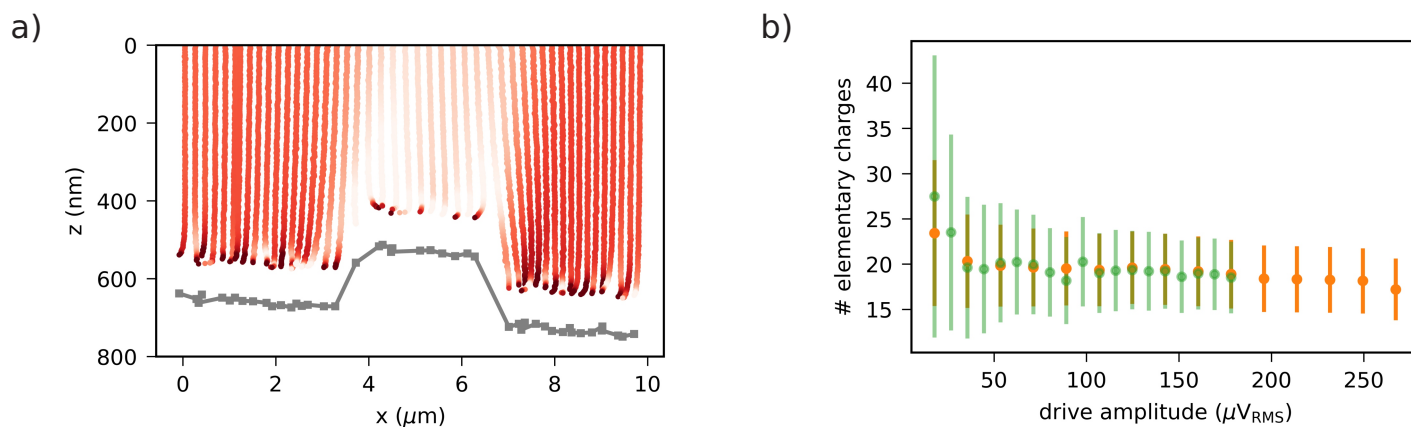
$$F_d = A(\omega_0)m\frac{\omega_0^2}{Q}. \quad (\text{S5})$$

We simulate the electrical field $E_{\text{sim}}(\mathbf{r})$ at a position $\mathbf{r} = (x, y, z)$ in COMSOL and use it to calculate the tip charge q_{tip} as

$$q_{\text{tip}} = F_d(\mathbf{r})/E_{\text{sim}}(\mathbf{r}). \quad (\text{S6})$$

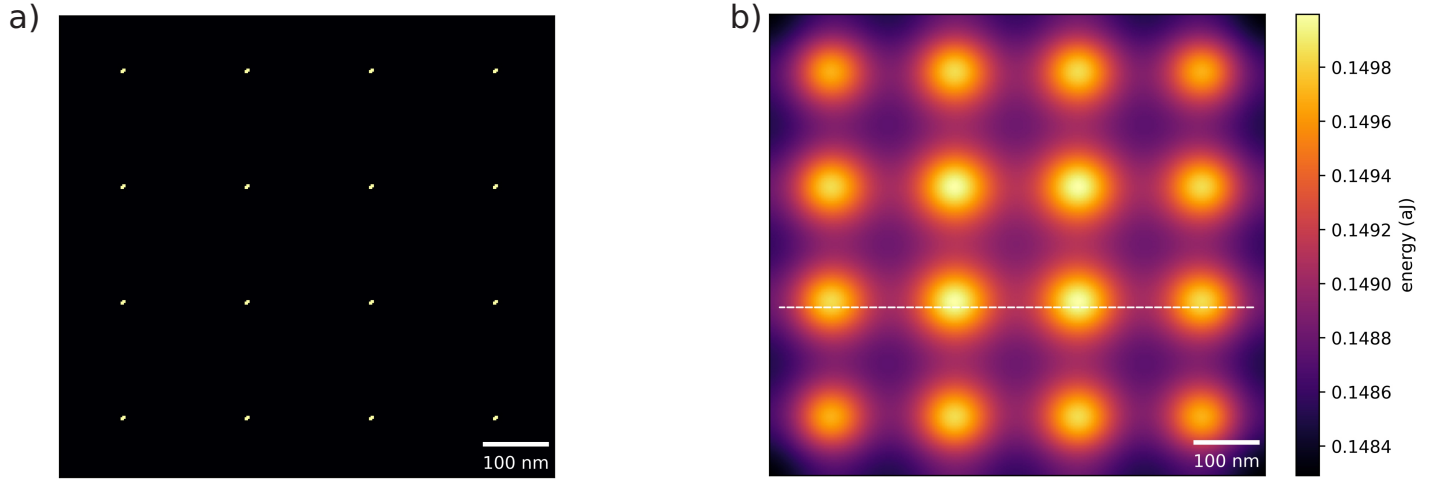
Note that the cantilever position must be carefully determined. When hovering over the stripline, we measure lateral shifts of several 10 – 100 nm compared to its nominal position, see Fig. S7(a). These shifts are monitored through changes in the feedback-controlled position of the cantilever in the interferometer fringe.^{S4} We further found that the force values measured on both side of the stripline differ, which we ascribe to a potential difference between the cantilever tip and our setup ground. We managed to cancel this effect by applying a DC voltage of 1.6 V to the stripline, resulting in a symmetric response and an estimated charge number of $q_{\text{tip}} \approx 20$.

Our method overestimates the number of charges interacting with the sample surface during the scanning force microscopy experiments. The Coulomb electric field of a point charge decays as $1/d^2$ whereas the driving field generated by the $\approx 2 \mu\text{m}$ -broad stripline only starts to decrease as $1/d$ after a few micrometers. Our method therefore merely gives an upper boundary on the actual number of charges carried by the cantilever tip (within a few tens of nanometers from the apex).

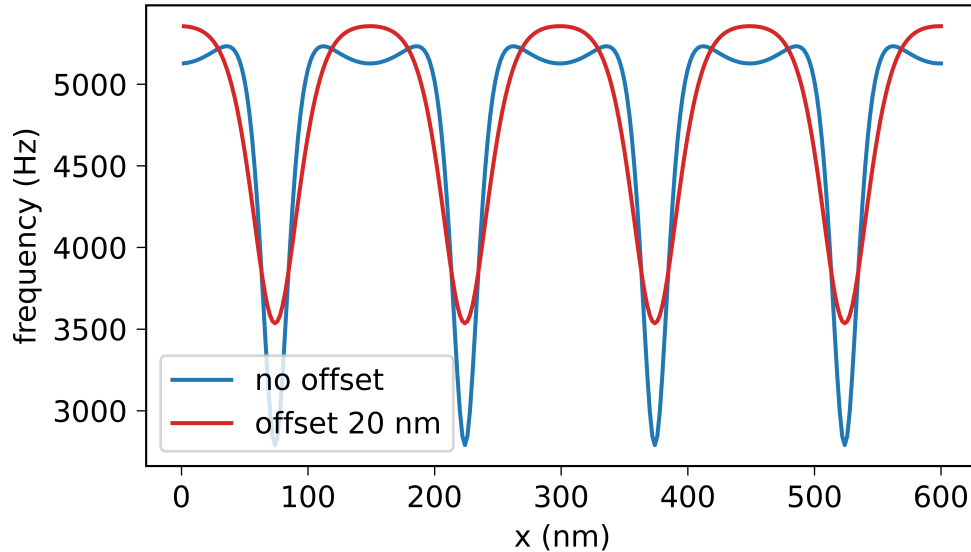


Supplementary Figure S7: (a) Cantilever static shift (lateral shift) and frequency (color coded: dark red 4.5 kHz, light red 5.5 kHz) for successive approaches above the sample. Grey points indicate the cantilever touch positions. The stripline profile is clearly visible. (b) Results of the charge calibration. The orange and green data is measured at the positions $x = 3.5 \mu\text{m}$ and $x = 6.5 \mu\text{m}$ in (a), respectively.

Electrostatic model



Supplementary Figure S8: (a) Simple charge density model. A charge q_i is placed at each white dot. (b) Energy map corresponding to $q_{\text{tip}} = q_e$ and $q_i = 0.7q_e$ at a surface-charge distance $d + \Delta = 50$ nm. The dashed line shows the position of the line scan in Fig. S9.



Supplementary Figure S9: Calculated frequency along the white dashed line in Fig. S8(b). The result for $d = 30$ nm without an offset is shown in blue, yielding a large asymmetry between the positive and negative frequency deviations and characteristic double maxima between charge sites that we do not observe in the experiment, cf. Fig 2(c) of the main text. Including a tip-charge offset of $\Delta = 20$ nm results in a much more realistic simulation.

In the main text, we explain the simple electrostatic model used to calculate the variable frequency

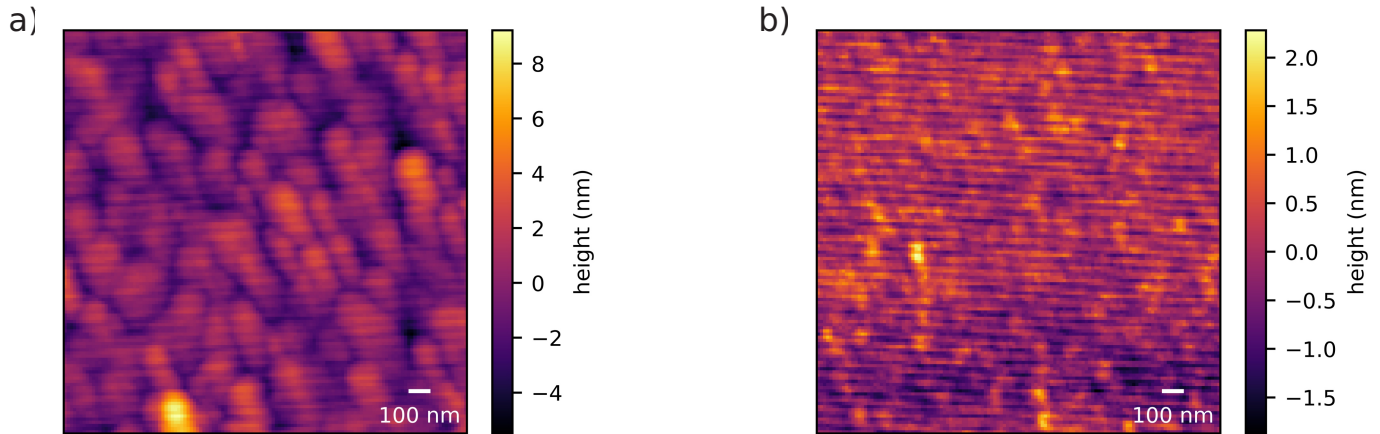
$$f = \frac{1}{2\pi} \sqrt{\frac{k_0}{m} + \frac{k_{\text{el}}}{m}}, \quad (\text{S7})$$

where $k_{\text{el}} = \delta^2 E_{\text{el}} / \delta x^2$ is the electrical spring constant obtained from the summed Coulomb energy of charges q_i on the surface. For the model comparison in Fig. 3, we placed charges on a grid with

a separation of 150 nm, see Fig. S8. To avoid edge effects, we simulate a 10×10 times larger area than that shown (i.e., evaluated). Two free parameters are involved in this simulation: first, we fix the value of $q_{\text{tip}}q_i = 0.7q_e^2$ by comparing the maximum and minimum frequencies found in a simulated line scan, see Fig. S9. Second, the characteristic asymmetry observed for $d = 30$ nm over Au provides us with a criterion to estimate the offset Δ between the tip apex and the effective charge position. For $\Delta = 0$, the model corresponds to a charge placed at the very apex, and the simulated line scan produces characteristic double peaks that are clearly absent in the experiment, see blue trace in Fig. S9. An offset of $\Delta = 20$ nm (± 5 nm) removes these double peaks, while preserving the asymmetry between the sharp dips and the broad maxima, see red trace in Fig. S9. The asymmetry stems from the difference between placing the tip directly over a repulsive charge (frequency dip) or at a position between two charges (frequency maximum). The offset is comparable to the nanowire tip radius of ~ 10 nm reported in an earlier publication.^{S5}

Surface topography images

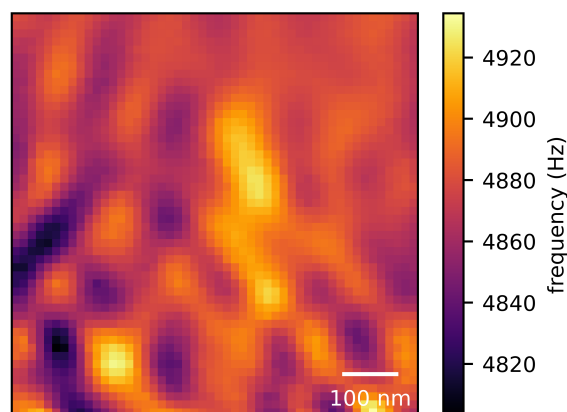
In Fig. S10, we display the surface topography of Au and SiO₂ on a second sample chip. The chip is cleaved from the same thermally oxidized Si wafer, and the Au layer was evaporated in the same process as for the sample mounted in our nanoladder scanning force microscope. The topography images in Fig. S10 were measured with a commercial atomic force microscope (AFM). They clearly show difference in topography between the two surfaces. In particular, the lateral grain sizes on Au are about 100 – 150 nm with a typical height of 4 – 6 nm, while those on SiO₂ appear to be smaller, roughly 20 – 50 nm laterally and 1 – 1.5 nm high. From these differences, we conclude it unlikely that the very similar frequency maps in Fig. 2(a)-(b) of the main text are directly caused by topographic variations.



Supplementary Figure S10: Surface topography of (a) Au and (b) SiO₂ surfaces on a second sample chip, measured with a commercial AFM.

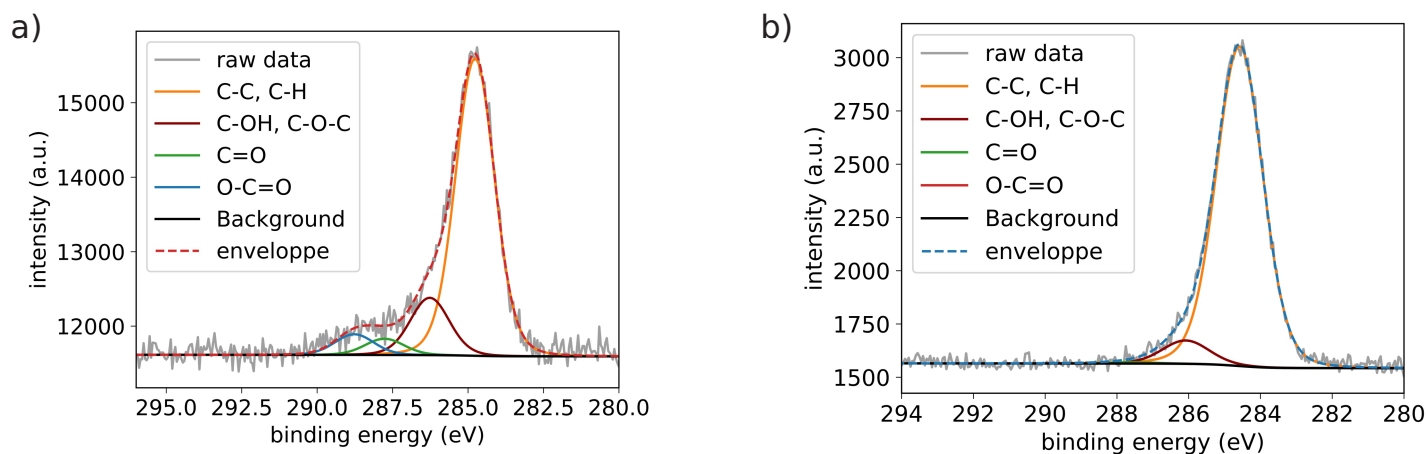
Frequency map over a different sample

In a separate experiment, we measured the cantilever frequency f over a 3 nm-thick Pt layer that was E-beam evaporated over diamond-like carbon, see Fig. S11. We observe a similar pattern as on Au and SiO₂, suggesting the presence of potential patches. We did not study the non-contact friction over this sample.



Supplementary Figure S11: Frequency map measured 50 nm over Pt.

XPS sample analysis



Supplementary Figure S12: Representative X-ray photoelectron spectra of (a) Au and (b) SiO₂ surfaces showing high-resolution C 1s regions. The shape of the spectra indicate that the composition of adsorbed hydrocarbon contamination differ between Au and SiO₂ surfaces. Specifically, deconvolution of the C 1s signals suggests a greater contribution of C-O bonding character in the thin layers of adventitious carbon material present on Au compared to SiO₂. The non-identical nature of the adsorbed material can lead to different dielectric parameters due to the additional interaction of permanent dipole moments in polar, oxygen-containing species with electric fields.^{S6}

We performed X-ray photoelectron spectroscopy using a PHI Quantera SXM photoelectron spectrometer at the Swiss Federal Laboratories for Materials Science and Technology (EMPA), see Fig. S12. A monochromatic Al K_αX-ray source with a 100 μm circular spot size was used under ultrahigh vacuum (1×10^{-9} mbar). High-resolution C 1s spectra were acquired at a pass energy of 55 eV using a 20 ms dwell time. For all scans, 15 kV was applied with an emission current of 3 mA; an average of 8-10 scans were collected per region. Spectra were fit with CasaXPS Software Version 2.3.23PR1.0 using a Shirley background and Gaussian-Lorentzian peak shapes to deconvolute contributions to the adventitious carbon signals. The dominant peaks were assigned to sp³ carbon and calibrated to 284.8 eV as a charge reference; satellite peaks at higher binding energies of ca. +1.5 eV and circa +3 – 4 eV were assigned to carbon singly and doubly bound to oxygen, respectively.^{S7} Relative signal contributions were averaged over spectra collected from three distinct regions for

both Au and SiO₂ surfaces.

References

- [S1]M. H eritier, A. Eichler, Y. Pan, U. Grob, I. Shorubalko, M. D. Krass, Y. Tao, and C. Degen, *Nano Letters*, 18, 1814 (2018), ISSN 1530-6984
- [S2]S. M. Yazdanian, J. A. Marohn, and R. F. Loring, *The Journal of Chemical Physics*, 128 (2008), ISSN 0021-9606
- [S3]S. Lekkala, J. A. Marohn, and R. F. Loring, *The Journal of chemical physics*, 139, 184702 (2013).
- [S4]U. Grob, M. D. Krass, M. H eritier, R. Pachlatko, J. Rhensius, J. Ko ata, B. A. Moores, H. Takahashi, A. Eichler, and C. L. Degen, *Nano Letters* 19, 7935 (2019), ISSN 1530-6984
- [S5]Y. Tao and C. L. Degen, *Nano Letters* 15, 7893 (2015), ISSN 1530-6984
- [S6]A. D. Sen, V. G. Anicich, and T. Arakelian, *Journal of Physics D: Applied Physics* 25, 516 (1992)
- [S7]S. Sangtawesin, B. L. Dwyer, S. Srinivasan, J. J. Allred, L. V. H. Rodgers, K. De Greve, A. Stacey, N. Dontschuk, K. M. O'Donnell, D. Hu, et al., *Phys. Rev. X* 9, 031052 (2019)